Enabling single-molecule localization microscopy in turbid food emulsions

Philosophical Transactions of the Royal Society. Series A, Mathematical, physical and engineering sciences
Jabermoradi, Abbas; Yang, Suyeon; Gobes, Martijn I.; Duynhoven, John P.M.; Hohlbein, Johannes
https://doi.org/10.1098/rsta.2020.0164

PHILOSOPHICAL TRANSACTIONS A

royalsocietypublishing.org/journal/rsta

Research

Cite this article: Jabermoradi A, Yang S, Gobes MI, van Duynhoven JPM, Hohlbein J. 2022 Enabling single-molecule localization microscopy in turbid food emulsions. *Phil. Trans. R. Soc. A* **380**: 20200164.
https://doi.org/10.1098/rsta.2020.0164

Received: 3 March 2021
Accepted: 20 August 2021

One contribution of 11 to a Theo Murphy meeting issue 'Super-resolution structured illumination microscopy (part 2)'.

Subject Areas:
physical chemistry, biophysics, light microscopy

Keywords:
adaptive optics, super-resolution microscopy, turbid media, colloids

Author for correspondence:
Johannes Hohlbein
e-mail: johannes.hohlbein@wur.nl

Electronic supplementary material is available online at https://doi.org/10.6084/m9.figshare.c.5789091.

Enabling single-molecule localization microscopy in turbid food emulsions

Abbas Jabermoradi[1], Suyeon Yang[1], Martijn I. Gobes[1], John P. M. van Duynhoven[1,3] and Johannes Hohlbein[1,2]

[1]Laboratory of Biophysics, and [2]Microspectroscopy Research Facility, Wageningen University and Research, Stippeneng 4, Wageningen 6708, The Netherlands
[3]Unilever Global Foods Innovation Centre, Bronland 14, Wageningen 6708, The Netherlands

AJ, 0000-0002-1112-6659; SY, 0000-0002-3233-4238; MIG, 0000-0003-4085-7749; JPMvD, 0000-0001-9769-0113; JH, 0000-0001-7436-2221

Turbidity poses a major challenge for the microscopic characterization of food systems. Local mismatches in refractive indices, for example, lead to significant image deterioration along sample depth. To mitigate the issue of turbidity and to increase the accessible optical resolution in food microscopy, we added adaptive optics (AO) and flat-field illumination to our previously published open microscopy framework, the miCube. In the detection path, we implemented AO via a deformable mirror to compensate aberrations and to modulate the emission wavefront enabling the engineering of point spread functions (PSFs) for single-molecule localization microscopy (SMLM) in three dimensions. As a model system for a non-transparent food colloid such as mayonnaise, we designed an oil-in-water emulsion containing the ferric ion binding protein phosvitin commonly present in egg yolk. We targeted phosvitin with fluorescently labelled primary antibodies and used PSF engineering to obtain two- and three-dimensional images of phosvitin covered oil droplets with sub 100 nm resolution. Our data indicated that phosvitin is homogeneously distributed at the interface. With the possibility to obtain super-resolved images in depth, our work paves the way for localizing biomacromolecules at heterogeneous colloidal interfaces in food emulsions.

THE ROYAL SOCIETY PUBLISHING

This article is part of the Theo Murphy meeting issue 'Super-resolution structured illumination microscopy (part 2)'.

1. Introduction

In turbid media, optical imaging can be compromised by the presence of ingredients or phases bearing different refractive indices. In food emulsion such as mayonnaise, for example, the presence of oil droplets in the aqueous phase will disturb incoming and outgoing wavefronts of light. With an increasing depth of imaging, more and more photons will be reflected, absorbed, or scattered leading to aberrated images that suffer from decreased resolution, blurriness and distortions [1,2]. To correct aberrations, the concept of adaptive optics (AO) was developed in which active controllable elements such as deformable mirrors or spatial light modulators allow to modulate the wavefronts before the light reaches the photon detecting camera [3]. First developed for astronomical telescopes [4], AO is increasingly finding applications in fluorescence microscopy such as a super-resolution [5], light-sheet [6], confocal [7,8] or multiphoton [9] microscopy. AO can be implemented using direct or indirect wavefront sensing [10]. In the direct sensing mode, an additional wavefront sensor (e.g. Shack–Hartmann wavefront sensor) is required to send instantaneous feedback to the optical element that can modulate the wavefront [11]. However, operation in direct mode reduces the number of photons available for image formation, hampering especially applications in single-molecule localization microscopy (SMLM) [12,13]. Using indirect sensing, the wavefront is obtained from analysing a sequence of images allowing more photons to reach the main camera and simplifying the experimental layout. A common implementation of indirect sensing AO uses a deformable mirror in reflecting mode to compensate aberrations that can be described by Zernike polynomials [14]. The deformable mirror consists of a number of tiltable micro-mirrors or actuators allowing to modulate individual sections of light in the Fourier plane.

In SMLM, individual emitters, whose distance to each other is below the diffraction limit, can be distinguished from each other, if conditions are achieved that allow separation of the emission of each fluorophore in time. In the dSTORM (direct stochastic optical reconstruction microscopy) variant, this requirement is achieved by using blinking fluorophores that switch between fluorescent and non-fluorescent states [15,16]. Originally, a two-dimensional imaging technique, three-dimensional resolution in SMLM can be achieved by breaking the axial symmetry of the imaged point spread function (PSF) using astigmatism [17,18] or further PSF engineering via phase masks or AO enabling saddle point, tetrapod [19] and double helix [20] PSFs. Our recent work introduced a method called circular-tangent phasor-based SMLM (ct-pSMLM) that enables fast and accurate localization of emitters after PSFs engineering on standard CPUs [21].

SMLM has not yet found widespread use to study food systems [22]. We therefore decided to update the previously published miCube microscopy framework [23] on several aspects to showcase SMLM in food-related turbid media. Quantitative SMLM measurements are often compromised by inhomogeneous illumination due to a Gaussian intensity distribution of the exciting laser beam. To overcome this issue, several approaches have been introduced to achieve illumination with a constant intensity over the entire field of view. Examples include the use of a pair of micro lenses array consisting of identical spherical lenslets [24,25], the use of multimode optical fibres for illumination (MMF) [26] in combination with speckle reducers [27] or rotating diffusers [28] with the latter being less suitable for total internal reflection fluorescence (TIRF) microscopy due to the degradation of spatial coherence that prevents diffraction limited focusing. Recent work further demonstrated flat field illumination over variable field sizes using two galvanometer scanning mirrors placed in a plane conjugated to the back focal plane of the microscope objective in epifluorescence or TIRF mode [29]. In our implementation, we added a top-hat beam shaper in the excitation path that converts the Gaussian shaped intensity distribution of the excitation beam into a homogeneous flat field profile (top hat) enabling

quantitative microscopy [30,31]. Moreover, we equipped the miCube with a deformable mirror placed in the detection pathway to compensate aberrations coming from in-depth imaging of opaque samples with spatial variations of refractive indices and for enabling PSF engineering. In particular, we adapted an approach called REALM (Robust and Effective Adaptive Optics in Localization Microscopy) that was recently developed to compensate aberrations in depth of complex biological samples [32]. REALM uses the image quality metric derived from a weighted sum of Fourier transforms of raw images of emitters to estimate the aberrations. REALM then compensates the aberrations of different Zernike modes based on the metric values and biases of the mirror.

In a recent study using conventional multi-colour confocal microscopy, we found evidence that the distribution of oxidized proteins in the water phase and the oil/water interface of mayonnaise is not homogeneous [33]. Mayonnaise is a highly turbid food emulsion containing up to 80% of oil, in which egg yolk acts as an emulsifier [34]. For the previous oxidation study, we saw structural features too small to be resolved, motivating us to implement SMLM. To demonstrate the applicability of SMLM, we will here use a dilute oil-in-water model emulsion that was emulsified with phosvitin [35]. Phosvitin is a protein contained in egg yolk that has a binding capacity for ferric ions [36]. Ferric/ferrous ions can catalyse lipid oxidation at the oil–water interface, which can be detrimental to the sensorial and nutritional quality of food emulsions. Visualization of phosvitin at oil–water interfaces in food emulsions is therefore relevant to understand lipid oxidation mechanisms and design anti-oxidant strategies [37]. For our model emulsion, we opted for a 15% v/v oil concentration to obtain small droplets (approx. 1 µm diameter) with a large surface area available for phosvitin. We then used a phosvitin antibody conjugated with the fluorophore Alexa Fluor 647 to map phosvitin at the droplet interface and to obtain the three-dimensional distribution of phosvitins. With the demonstration of SMLM supported by adaptive optics, PSF engineering and a flat-field illumination scheme, our work paves the way for quantitative characterization of food systems under ambient environmental conditions.

2. Material and methods

(a) The miCube excitation path

For laser excitation, we used one of two options. The first option features a standard laser combiner (Omicron Lighthub, Germany) equipped with four lasers operating at 405 nm, 488 nm, 561 nm and 642 nm that were coupled into a single-mode fibre. As a second option, we used two low-cost diode lasers equipped with simple beam shaping optics. The lasers operate at 635 nm (PD-01287, 200 mW, Standard Module, Lasertack, Germany) and 520 nm (PD-01298, 100 mW, Standard Module, Lasertack, Germany) and are controlled via a home-built Arduino powered laser control engine (hohlbeinlab.github.io/miCube/LaserTrack_Arduino.html). After combining the laser light with a dichroic mirror (RGB Beam Splitter-Combiner, Lasertack, Germany), the light was coupled into a single-mode fibre (P3-460B-FC-2, Thorlabs) using a 10× objective (RMS10X - 10X Olympus Plan Achromat Objective, Japan). The coupling efficiencies of the 635 nm and 520 nm diode lasers to single-mode fibre were 56% and 42%, respectively. For collimating the laser light after the fibre, we used an achromatic lens (CL) of either 30 mm or 60 mm focal length (AC254-030-A-ML and AC254-060-A-ML, Thorlabs). Collimation was checked with a shear plate (SI050, Thorlabs). The laser light was then reflected by an elliptical mirror (M1, BBE1-E02, Thorlabs) mounted to a right-angle kinematic cage mount (KCB1E/M, Thorlabs), towards the top-hat beam shaper (TSM25-10-D-D-355, Top Shape, Asphericon GmbH, Germany) to create a homogeneous distribution of illumination intensity. The ideal input beam size for the beam shaper is between 9.2 mm and 10.8 mm ($1/e^2$). Using the 60 mm collimating lens, the input beam size is approximately 10.2 mm. After the beam shaping, the laser beam was reflected with another mirror (M2, BBE1-E02, Thorlabs) towards an iris (Iris, SM1D12D, Thorlabs) that allows the area of illumination in the sample plane to be controlled. The laser light was then focused into the back focal plane (BFP) of the microscope objective using an achromatic lens (TR,

$f = 150$ mm, AC508-150-A-ML, Thorlabs) mounted on a translational stage (XR25C/M, Thorlabs) used to change the position of the focus in the BFP.

(b) The miCube main block

The main block itself is similar to the one reported previously [23]. The laser beam focused by the TIRF lens is reflected by a polychroic mirror (DiM, ZT532/640rpc or ZT405/488/561/640rpcv2, Chroma) into the back focal plane of the objective lens (OL, CFI Plan Apo Lambda 100× Oil NA 1.45, Nikon). The sample was placed on a three-dimensional printed coverslip sample holder and secured in place with small magnets. We used a stick–slip piezo *XYZ* stage (SLS-3232, SmarAct GmbH, Germany) for sample scanning. The stage has a footprint of 32 mm by 32 mm and offers a travel range of 21 mm in each direction with 1 nm closed-loop resolvable position resolution. The stage is able to handle payloads of up to 1.5 N. The light emitted from the sample was collected with the same microscope objective and, after passing the polychroic mirror, further cleaned up with a bandpass filter (F, ZET532/640m-TRF, Chroma) located at the bottom of the dichroic cage holder (DFM1/M, Thorlabs) to block remaining back-reflected laser light from entering the emission path. Subsequently, emitted light was reflected using a 90° mirror (M3, BBE1-E02, Thorlabs) towards the tube lens.

(c) The miCube emission path

A tube lens TuL (MXA20696, Nikon) with 200 mm effective focal length is used to form an image in the first image plane. An elliptical mirror M4 (BBE1-E02, Thorlabs) steers the light towards a 4f system of lenses. The first lens L1 (AC508-100-A-ML, Thorlabs) was positioned to collimate the light from the first image plane. As the angle between incident and reflected light from the deformable mirror should stay below 30°, we used mirror M5 (PF10-03-P01, Protected Silver Mirror, Thorlabs) mounted to a precision kinematic mirror holder (KS1, Thorlabs), placed in front of the deformable mirror to control this angle. For modifying the incoming wave front and to compensate the aberrations, we placed the deformable mirror DM (DMP40/M-P01, 40-Actuator Piezo Deformable Mirror, Thorlabs) in the Fourier plane of L1 (one focal distance). The deformable mirror consists of a 40-actuator array with three bimorph benders for ±2.0 mrad Tip/Tilt actuation and was mounted on a *XZ* linear stage (XR25C/M, Thorlabs) to simplify the alignment of the mirror in respect to the emission light. The light reflected from the deformable mirror was conducted to lens L2 (AC508-100-A-ML, Thorlabs), which focused the light on the camera (Prime 95B sCMOS, Photometrics) having a maximum quantum yield of 95% QE and featuring a 11 µm by 11 µm pixel size. The camera was mounted on a custom three-dimensional printed stand to adjust the height and position on the optical table.

(d) Rescan-confocal microscopy

We updated the previous miCube microscope with a rescan-confocal microscopy (RCM) module (Confocal.nl, Amsterdam, The Netherlands) [38]. The RCM has a separate fibre input for and allows scanning of the collimated laser beam across the sample. The emitted light from the specimen is then rescanned with a second mirror with twice the sweep length as the excitation scanning mirror, leading to a 43 nm pixel size on the sCMOS chip. The RCM is capable of achieving a $\sqrt{2}$ times increase in resolution compared to classical confocal laser scanning microscopes.

(e) Deformable mirror for adaptive optics and PSF engineering

The mirror (DM, DMP40/M-P01, 40-Actuator Piezo Deformable Mirror, Thorlabs) consists of 40 individual actuators and three arms for tip/tilt. Each actuator and each arm can be controlled by applying voltages between 0 V and 200 V. In combination, the voltages determine the

curvature of the mirror. To correct the flatness of the mirror and later for modulating the PSFs, we implemented REALM (github.com/MSiemons/REALM) [32], which allows for corrections without requiring an additional sensor to monitor the incoming wavefront. We further wrote a plugin for Micromanager to connect REALM to the deformable mirror used in our study (github.com/HohlbeinLab/Thorlabs_DM_Device_Adapter) [21].

(f) Data acquisition, visualization and image analysis of SMLM data

If not stated otherwise, we used the 642 nm laser for excitation of Alexa Fluor 647 and the 405 nm laser for photo-reactivation. Movies were recorded for 10 000 frames with a frame time of 20 ms.

The raw data were analysed with ThunderSTORM [39] plugin in ImageJ/Fiji [40] based on the phasor-based localization algorithm [41]. After obtaining the localizations, we performed two-dimensional cross-correlation drift correction (settings in ThunderSTORM: 10 bins and 5× magnification). The localizations were visualized using the average shifted histogram options, with the magnification set to 5. Moreover, no lateral shifts were added and cyan was chosen for the lookup table. A rewritten ImageJ plugin was used to remove constant fluorescence background by means of a temporal median filter [42] (see github.com/HohlbeinLab/FTM2 for the ImageJ/Fiji plugin). To determine the histogram of droplet sizes, we first manually encircled droplets in the field of view based on the ring-shaped presence and absence of fluorescence. We then applied the Hough circle transform [43] function in MATLAB (Mathworks, UK) to obtain the radii of all circles using 0.2 µm as the minimum and 2 µm as the maximum search radius for oil droplets. For measuring the resolution of super resolved images, we further used Fourier Ring Correlation (FRC) as implemented in the software package SMAP [44].

(g) Isolation and purification of phosvitin

Our procedure of isolating and purifying phosvitin follows previous work [36]. Briefly, fresh hen eggs were purchased from the domestic market. To remove egg white and chalazas, the yolks were rolled on a filter paper. The temperature of the following steps was kept at 4°C. An equal amount of distilled water was added to the yolk. The diluted solution was centrifuged at 12 000*g* for 10 min (Avanti j-25, Beckman). The precipitate was collected and homogenized with an equal mass of a 0.17 M NaCl solution and centrifuged again at 12 000*g* for 10 min. The granules were dissolved in a 10% w/v of a 1.74 M NaCl solution. The pH was adjusted to 8.0 with 1 mM NaOH solution and homogenized with 4% PEG6000 w/w and centrifuged at 12 000*g* for another 10 min. The supernatant was dialysed against distilled water for 48 h and subsequently centrifuged at 12 000*g* for 10 min. The supernatant was collected and lyophilized using a lyophilizer from either Christ, Germany or Labconco, USA.

(h) Phosvitin-based model emulsion

In total, 6 mg ml^{-1} of lyophilized phosvitin was added to 0.05 M of 2-*N*-porpholino ethane sulfonic acid (MES) buffer at pH 6.6. The solution was centrifuged at 4000*g* for 20 min and the supernatant was extracted to remove the undissolved particle from the solution. We then added 0.15% w/v of sodium dodecyl sulfate (SDS) to the solution to obtain a stable model emulsion. A 15% oil in water mixture was prepared with 7.5 ml of rapeseed oil and 42.5 ml of the phosvitin containing solution. The emulsion was premixed with an 18 mm diameter head disperser at 18 000 r.p.m. for 2 min (T 18 digital ULTRA-TURRAX, IKA, Germany). Next, the 15% oil in water model emulsion was obtained by emulsifying the premix at 70 bar for 20 min with a flow rate of 80 ml min^{-1} using a high-pressure homogenizer (Delta Instruments LAB Homogenizer).

(i) Sample preparation

For the rescan-confocal microscopy measurements on mayonnaise, 1% w/w of 1 mg ml^{-1} Nile blue (Sigma, ref. N0766) solution was gently stirred into the mayonnaise. Nile blue was excited

at 642 nm. For correcting the deformable mirror, we used fluorescent beads (FluoSpheres™ Carboxylate-Modified Microspheres, 28 nm diameter, dark red fluorescent (660/680), Thermo Fisher). First, we diluted the provided solution 1 : 100 000 and added 4 ml of the dilution to a coverslip (no. 1.5, Thermo Scientific Menzel Gläser). We then used a second coverslip used on top of the first one to have homogeneous distribution of beads on the field of view. To measure the drift characteristics in x, y and z, we prepared a sample as described but using 50 nm fluorescent beads (560 nm peak emission wavelength) instead. For dSTORM measurements, the phosvitin antibody conjugated with Alexa Fluor 647 stock solution was first diluted 50 times in TRIS buffer. Here 40 µl of the diluted antibodies were then added to 400 µl of the 15% oil-in-water model emulsion. In order to stall self-diffusion of droplets, we further added 0.5% w/v of guar gum (Sigma, ref. G4129). The specimen was then dripped into a well of a silicon gasket. 1.5 µl of the STORM buffer containing 50 mM TRIS pH8, 10 mM NaCl, 10% glucose, 140 mM 2-mercaptoethanol, 68 µg ml^{-1} catalase and 200 µg ml^{-1} glucose oxidase [45] was mixed into 15 µl of sample, before we sealed the gasket. We note that although we effectively used a 10-fold reduced concentration of a standard STORM buffer in our sample, sufficient blinking was achieved. Using a 10× increased concentration of BME did not lead to improvements in blinking and achievable resolution.

3. Results and discussion

(a) Turbidity compromises the image quality in oil-in-water emulsions

We first imaged a mayonnaise sample containing Nile blue using a stack of confocal images to demonstrate the challenges of optical imaging in turbid media (figure 1*a*). The expected loss of optical resolution in depth of the sample is seen in the cross-sectional view; an increase of imaging depth coincides with increased blurriness (figure 1*b*,*c*). To obtain a model emulsion suitable for SMLM, we prepared a low (15%) oil-in-water model emulsion emulsified with phosvitin. We decided to start with a simple model system consisting of phosvitin as the main emulsifier to develop and refine the required microscopy framework. The main restriction of using real mayonnaise is its compositional complexity: egg yolk, used as emulsifier in mayonnaise, consists of many different proteins (e.g. phosvitin, LDL, ApoB) making an attribution of the individual contributions difficult. Owing to the lower oil content of the model emulsion, the packing of droplets is less dense leading to self-diffusion of droplets. We therefore added guar gum to the emulsion which increased the viscosity leading to an effective immobilization of the droplets. The rescan-confocal laser scanning images showed that the high shear during emulsification resulted in smaller droplet sizes (approx. 0.5 µm radius) compared to typical mayonnaises (2–2.5 µm radius; figure 1*d*). Similar to imaging in mayonnaise, we observed a loss of resolution and signal-to-noise ratio with increasing depth (figure 1). We note that larger areas are void of droplets and are likely occupied with guar gum networks (figure 1*e*,*f*: xz and xy sectional views).

(b) Adapting the miCube for SMLM in turbid media

We modified the miCube microscopy framework [23] at various positions to address the challenges imposed by super-resolution measurements in turbid media and to provide users with additional hardware options (figure 2). In the excitation path, we included an option to use cheaper laser diodes as light sources rather than a scientific-grade multicolour laser engine. To enable simplified quantitative analysis of super-resolution data, we added a top-hat beam shaper providing an even illumination profile over the field of view [24,30,31]. We compared the resulting illumination profile in the field of view with one obtained using conventional Gaussian distributed laser excitation (figure 2*b*–*d*). To this end, we placed a droplet of 1 µM Cy3B dye solution (Cytiva) on the coverslip and used a second coverslip on top to obtain a homogeneous spatial distribution of fluorophores. The fluorescence intensity profiles of the Gaussian and flat-top epi-illumination were obtained by exciting the sample with the 561 nm laser set to 26 mW.

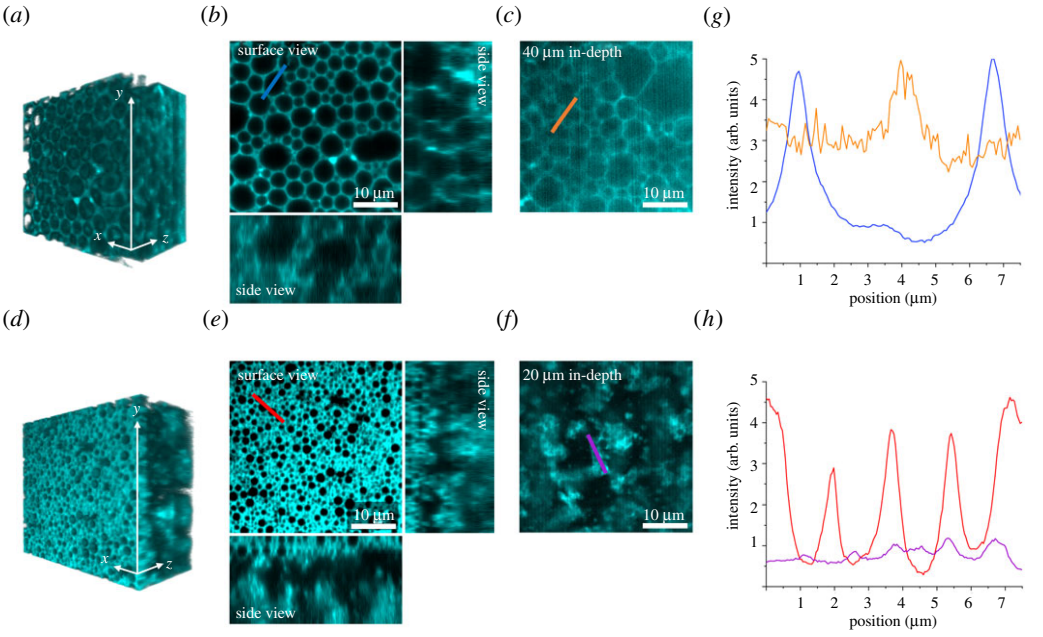

Figure 1. Rescan-confocal images of mayonnaise and the model emulsion labelled with Nile blue. (*a*) Three-dimensional volume rendering image of 40 µm by 40 µm by 20 µm taken with a 1 µm step size along the optical *z*-axis. (*b*,*c*) Cross-sectional views in different planes of *xy-xz-yz* shows in a slice of 20 µm thickness (*b*) and in the *xy* plane located in 40 µm depth in the sample (*c*). (*d*) Three-dimensional volume rendering of 40 µm by 40 µm by 20 µm stabilized by guar gum, taken with 1 µm step size. (*e*,*f*) Cross-sectional views in different planes of *xy-xz-yz* starting at the surface close to the coverslip (*e*) and in the *xy* plane located in 20 µm depth in the sample (*f*). Void areas in the model emulsion are caused by the guar gum network. (*g*) Line plots of fluorescence intensity (blue line in *b*) representing the achievable signal to noise of droplets close to the glass interface and (orange line in *c*) in 40 µm depth. (*h*) Line plots of fluorescence intensity (red line in *e*) representing the achievable signal to noise of droplets close to the glass interface and (purple line in *f*) in 20 µm depth. (Online version in colour.)

Using a collimating lens with a focal length of CL = 30 mm and 60 mm (for their position, see figure 2), we achieved a full width at 90% of the maximum intensity (FW90M) for these two lenses in the Gaussian illumination mode of 27 µm and 28 µm and for flat illumination of 116 µm and 128 µm, respectively (figure 2*d*). The flat field leads to laser intensity of 0.19 kW cm^{-2}.

For the main cube, we opted for a sample scanning stage that offers nanometer resolution over a 21 mm scanning range in all three directions and working in closed loop mode to compensate the thermal drift of the stage (electronic supplementary material, figure S1).

In the detection path, we implemented a deformable mirror to correct the aberrations induced by either the sample or by other optical elements in the detection pathway and enable PSF engineering that allow us to have higher *z* range in three dimensions. We noted, however, that the deformable mirror itself introduces additional aberrations to the system requiring corrections. Using the standard setting of all actuators set to 100 V, we observed asymmetrically elongated PSFs (figure 2*e*) rather than the expected symmetrical and circular PSFs when imaging fluorescent latex beads of 28 nm diameter. To correct the flatness of the mirror and later for modulating the PSFs, we implemented REALM [32]. Using REALM, each Zernike aberration mode was individually corrected by sequentially optimizing the image metric (figure 2*f*). The software evaluated 11 biases ranging from −100 nm to 100 nm for the mirror setting for each of the nine tested Zernike modes. By using three correction rounds, a total of 297 images were acquired. A Gaussian function was fitted to the metric values of each bias. The position of the maximum of the fitted function was taken as the required correction amplitude for that specific mode. After

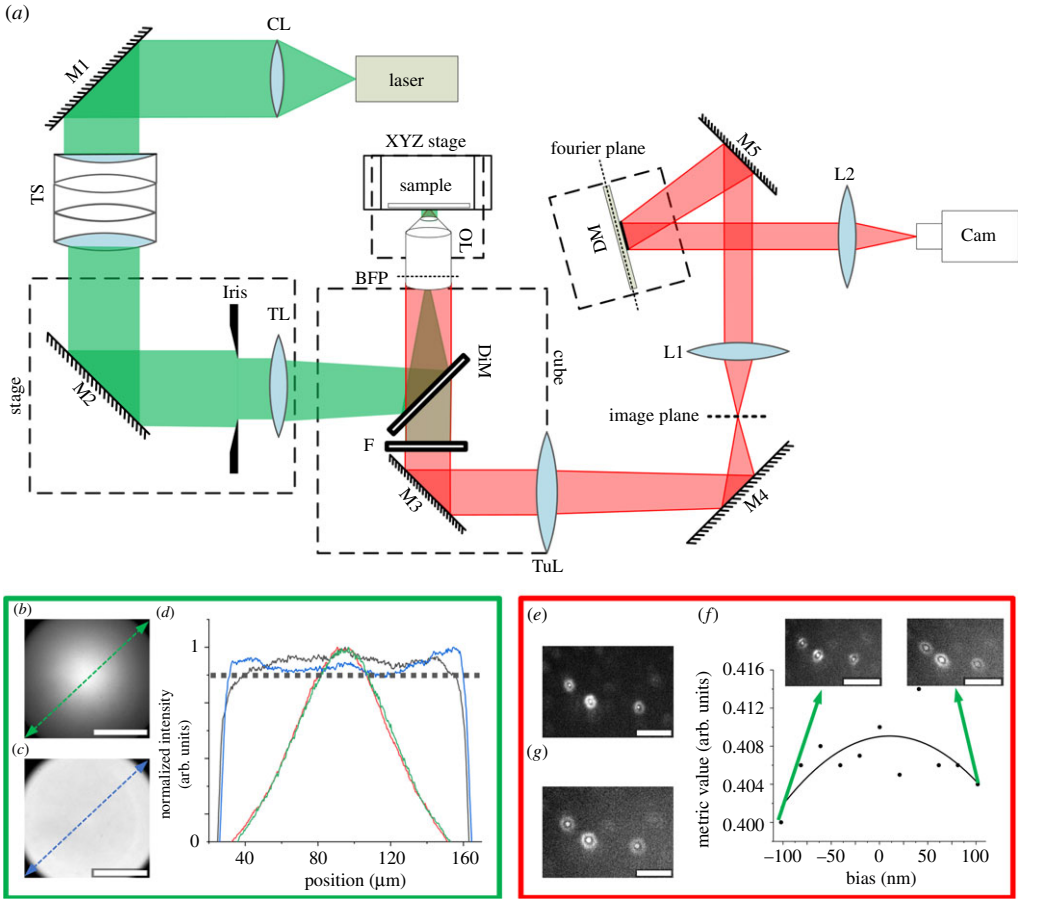

Figure 2. (*a*) Schematic of the optical pathway. The excitation path (left, green) and the detection path (right, red) are highlighted. Components include a collimating lens (CL), mirrors (M), top-hat beam shaper (TS), TIRF lens (TL), polychroic mirror (DiM), objective lens (OL), back focal plane (BFP), bandpass filter (F), tube lens (TuL), lenses (L), deformable mirror (DM), and a camera (Cam). (*b–d*) Characterization of the intensity profile in the field of view. Two collimating lenses (CL) were compared with either 30 mm or 60 mm focal length and with or without top-hat beam shaper. (*b*) Intensity profile after using the 60 mm lens. (*c*) Intensity profile after using the 60 mm lens with added top-hat beam shaper. Scale bars in (*b*,*c*) represent 50 μm. (*d*) The line profiles of *b* (green line) and *c* (blue line) are plotted and compared to using the 30 mm collimation lens with (black line) and without the top-hat beam shaper (red line). (*e*,*f*) Corrections of aberrations using adaptive optics in the emission path. (*e*) Fluorescent beads (28 nm diameter) were immobilized on a cover slip and imaged. Here, the asymmetrical shape of the PSF is induced by the deformable mirror itself. (*f*) A specific Zernike mode, oblique secondary astigmatism $-Z(4, -2)$, was selected and the correction procedure was performed providing a Gaussian fit of the obtained metric values and biases. (*g*) The expected symmetrical shape of the PSF is restored after correcting the deformable mirror for all Zernike modes using REALM. We note that the beads are slightly out of focus to exemplify the symmetry. Scale bars in (*e–g*) represent 10 μm. (Online version in colour.)

correcting the mirror, the expected circular symmetry of the PSF is restored (figure 2*g*) and we found the correction settings to be stable for several months.

(c) Super-resolution microscopy in turbid media

Phosvitin is an egg yolk protein that has a binding capacity for ferric ions [36] which can catalyse lipid oxidation at oil–water interface in food emulsions. Here, we aimed at visualizing phosvitin at the oil–water interfaces of a model emulsion to explore the potential spatial heterogeneity of

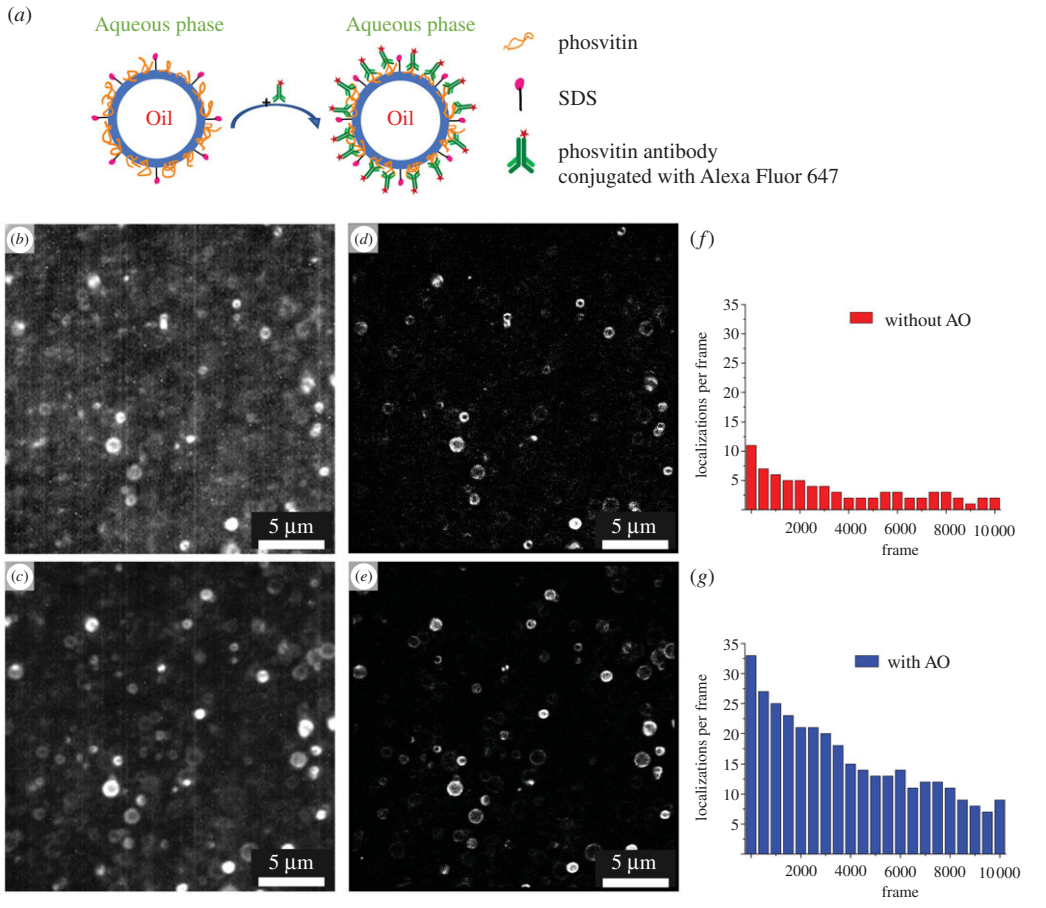

Figure 3. From diffraction limited to super-resolved imaging of fluorescently labelled antibodies bound to phosvitin present at the oil–water interface of a model food emulsion. (*a*) Schematic diagram of an oil-in-water emulsion droplet in the model emulsion. Phosvitin and SDS jointly stabilize the oil–water interface. We then added antibodies against phosvitin that are fluorescently labelled (Alexa Fluor 647) to localize phosvitin at the interface using dSTORM. (*b–e*) Comparing diffraction limited and super-resolved images with and without adaptive optics. (*b,c*) The accumulated fluorescence intensity over 10 000 frames each in the same field of view in 8 µm sample depth first measured without (*b*) and then with AO enabled (*c*). (*d,e*) The corresponding super-resolved images of the same stack in 8 µm sample depth without (*d*) and with AO enabled (*e*). (*f,g*) The number of localizations in the field of view per 500 frames without (*f*) and with AO (*g*). (Online version in colour.)

phosvitin that could provide clues to design strategies combating lipid oxidation. In our 15% oil-in-water model emulsion, phosvitin took the role as the main emulsifier. We further added SDS to increase the stability of the emulsion (figure 3*a*). To localize phosvitin at the oil–water interface, we added fluorescently labelled antibodies against phosvitin.

To demonstrate the effect of adaptive optics, we first recorded data in 8 µm depth without aberration correction in addition to the flat-mirror correction with REALM (figure 3*b–d*) for 5 min. Then, the sample was imaged with the depth correction setting applied. The outlines of the oil droplets representing labelled antibodies bound to phosvitin are clearly visible. We performed control experiments with phalloidin antibodies conjugated with Alexa Fluor 647 to verify the specificity of the phosvitin antibodies. As expected, a noisy background was observed without clear outlines of droplets being visible (electronic supplementary material, figure S2). Before any further analysis of the raw data, we minimized the influence of background fluorescence by applying a temporal median filter (see Material and methods). To compare the datasets with and without aberration correction, we first summed up the intensities of all 10 000

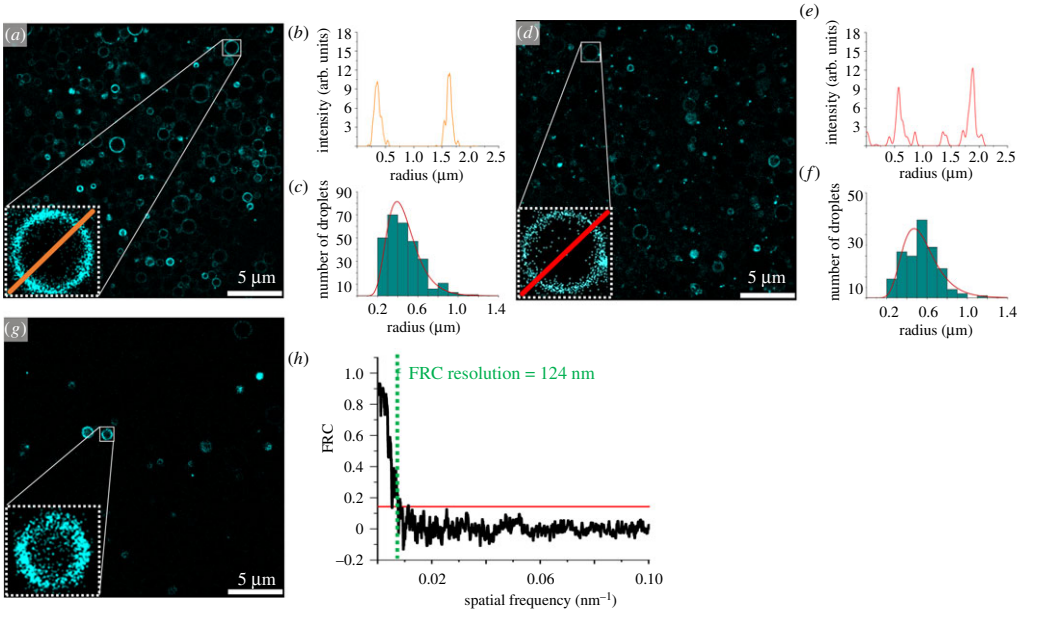

Figure 4. Superresolved imaging in various depths of a turbid model food emulsion. (*a*,*d*,*g*) 25 µm by 25 µm field of view of the super-resolved droplets (*a*) close (less than 1 µm) to the surface, (*d*) 4 µm in-depth and, (*g*) 15 µm in-depth. Line profile of an enlarged droplet from the sample with a radius of (*b*) approximately 0.65 µm and (*e*) approximately 0.75 µm. Apparent size distributions presented as histograms for a 15% model emulsion stabilized with phosvitin for the plane close to the surface (*c*) and, the plane 4 µm in-depth (*f*). (*h*) The FRC calculation to determine the resolution of super resolved image in 15 µm depth. (Online version in colour.)

frames pixel by pixel to mimic diffraction-limited resolution (figure 3*b*,*c*). With correction, more droplets are visible showing a clear circular shape with better signal-to-noise ratio. We then analysed the individual point spread functions frame by frame to demonstrate the increase in resolution obtainable in SMLM (figure 3*d*,*e*). As indicated in the histograms, more localizations per movie frame can be obtained after correction with AO due to a better signal-to-noise ratio (figure 3*f*,*g*).

For a more quantitative analysis, we then imaged a new sample in a plane close to the surface (a few 100 nm deep) and plotted a line profile over an isolated droplet (figure 4*a*) indicating a radii of approximately 0.65 µm. Further, analysing the profile of the droplet using a Gaussian fit and calculating the FWHM of the intensity profile around the droplets revealed a thickness of 74 nm (electronic supplementary material, figure S3) thereby representing a convolution of the localization precision and the expected geometrical averaging due to projecting a three-dimensional cut-out of a sphere onto a two-dimensional imaging plane. We obtained an imaging resolution of 71 nm using FRC [42,44,46] (electronic supplementary material, figure S4). In total, we found 284 droplets with radii between 0.2 µm and 1.2 µm with a number averaged mean radius of 0.46 µm (figure 4*c* and electronic supplementary material, figure S5). We note that these are apparent radii due to the error introduced by the imaging plane not crossing all droplets at the centre [47].

We then recorded data in 4 µm depth (figure 4*d*) after applying the aberration corrections obtained with REALM. At this depth, the PSFs of individual fluorophore emitters are only slightly aberrated such that they could be directly used to obtain the correction coefficients. We again enlarged a droplet and obtained a radius of 0.75 µm. In this plane, we obtained 79 nm for the FWHM of the intensity profile around the droplet (electronic supplementary material, figure S3). We counted 134 droplets with a different radius between 0.2 µm and 1.8 µm and a number averaged mean of 0.55 µm (figure 4*f* and electronic supplementary material, figure S5).

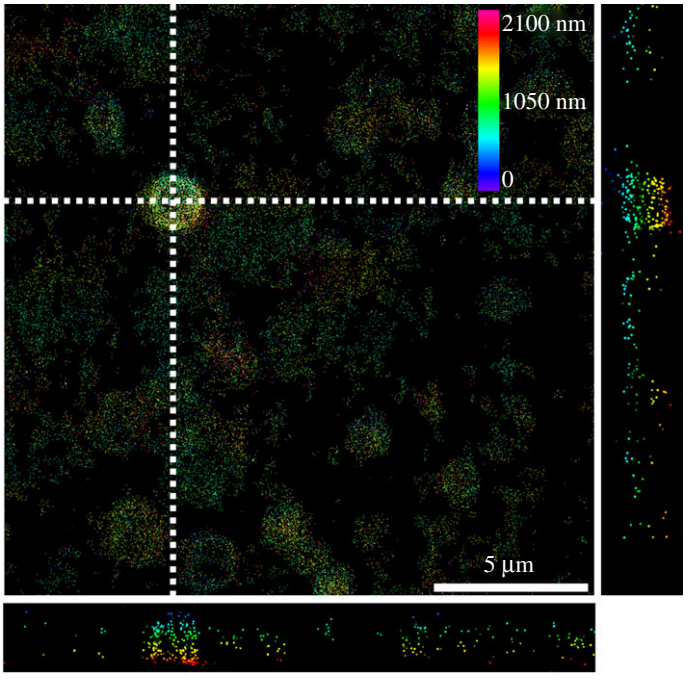

Figure 5. 20 µm × 20 µm image of the oil-in-water model emulsion droplets in 4 µm depth with the saddle point PSF setting providing a 2.1 µm *z*-range. The cross-sectional views show the distribution of protein in the *xz*- and *xy*-plane. Saddle point PSFs were introduced by applying vertical astigmatism and vertical secondary astigmatism Zernike modes to the deformable mirror. (Online version in colour.)

At 15 µm sample depth we had to first correct the PSFs using embedded fluorescent latex beads. We further had to increase the laser excitation power twofold to obtain a sufficient number of photons per localization (figure 4*g*). As we measured deeper into the sample, we noticed a decrease in the number of droplets present likely induced by the guar gum used to reduce the mobility of droplets in the sample. We achieved super resolved images in 15 µm depth indicated by resolving two droplets with approximately 0.45 µm radius. Using FRC, we calculated the resolution of the image to be approximately 124 nm (figure 4*h*). As expected, the number of droplets per field of view reduced to 27 with an averaged mean radius of 0.43 µm and mostly those droplets distributed between 0.35 µm and 0.48 µm. We note that the operational range offered by SMLM is not accessible by conventional laser scanning microscopy, which typically has a lower limit of 0.5 µm for determining the radii of droplets [48].

(d) Obtaining three-dimensional image of oil droplets using PSF engineering

To show the capability of three-dimensional imaging using adaptive optics, we recorded engineered PSFs using the deformable mirror. Various PSFs such as astigmatism, saddle point and tetrapod can be engineered using the deformable mirror. To access a 2–2.5 µm *z*-range, we employed vertical astigmatism and vertical secondary astigmatism Zernike coefficients (Saddle point PSF). We recorded 40 000 frames with 30 ms frame time (figure 5). We visualized the cross-sectional view of three-dimensional distribution in *xz*- and *yz*-planes, showing that the full volume of a droplet can be covered and further indicating that phosvitin is homogeneously distributed at oil droplet interfaces. Vertical and horizontal dashed lines in figure 5 indicate the corresponding *xz* and *yz* sections. We note that further analysis of the homogeneity will critically depend on the surface coverage of the droplets with phosvitin and the matching, fluorescently labelled antibody.

4. Conclusion

In this study, we presented an updated design of the miCube open-source microscope featuring flat-field illumination and adaptive optics for PSF engineering. Together, these updates enable 3D-SMLM in both standard samples and samples compromised by inherent turbidity. As a first model system we used a dilute oil-in-water emulsion in which we imaged the iron-binding protein phosvitin at the droplet interface using a primary phosvitin antibody conjugated with Alexa Fluor 647. Flat-field illumination enables homogeneous excitation intensities over areas surpassing 30 µm by 30 µm indicating that phosvitin is homogeneously distributed over the droplet interfaces. Droplets with radii as small as 0.2 µm can be discerned and localization of phosvitin in extended sample depths is possible. Using the deformable mirror to engineer PSFs, we demonstrated that extended z-ranges can be accessed with SMLM without moving the focus of the objective in the sample plane. Our work showed the ability of the open miCube platform to perform SMLM techniques for localizing biomacromolecules in both two and three dimensions at colloidal interfaces in complex and oxidation-sensitive food emulsions.

Data accessibility. The experimental raw data are available on https://zenodo.org/record/5019187#.YegvQf7P2Uk.

Authors' contributions. A.J.: methodology, software, validation, investigation, data curation, drafting the manuscript, writing-review and editing, visualization. S.Y.: investigation, data curation. M.G.: software. J.P.M.v.D.: conceptualization, methodology, validation, writing-review and editing, supervision, funding acquisition. J.H.: conceptualization, methodology, validation, writing-review and editing, supervision, funding acquisition.

Competing interests. J.P.M.v.D. is employed by a company that manufactures and markets mayonnaise. The other authors declare that they have no known competing financial interests or personal relationships that could influence the work reported in this paper.

Funding. This work is part of the research programs LocalBioFood and LICENSE with project nos. 731.017.204 and 731.017.301, which are financed by the Dutch Research Council (NWO).

Acknowledgements. We would like to thank our colleagues in both consortia (LocalBioFood and LICENSE) and the Laboratory of Biophysics for helpful discussions.

References

1. Schwertner M, Booth MJ, Wilson T. 2004 Characterizing specimen induced aberrations for high NA adaptive optical microscopy. *Opt. Express* **12**, 6540–6552. (doi:10.1364/OPEX.12.006540)
2. Vellekoop IM, Aegerter CM. 2010 Scattered light fluorescence microscopy: imaging through turbid layers. *Opt. Lett.* **35**, 1245–1247. (doi:10.1364/OL.35.001245)
3. Girkin JM, Poland S, Wright AJ. 2009 Adaptive optics for deeper imaging of biological samples. *Curr. Opin Biotechnol.* **20**, 106–110. (doi:10.1016/j.copbio.2009.02.009)
4. Hardy JW. 1998 *Adaptive optics for astronomical telescopes*. Oxford, UK: Oxford University Press.
5. Booth M, Andrade D, Burke D, Patton B, Zurauskas M. 2015 Aberrations and adaptive optics in super-resolution microscopy. *Microscopy* **64**, 251–261. (doi:10.1093/jmicro/dfv033)
6. Dalgarno HIC, Čižmár T, Vettenburg T, Nylk J, Gunn-Moore FJ, Dholakia K. 2012 Wavefront corrected light sheet microscopy in turbid media. *Appl. Phys. Lett.* **100**, 191108. (doi:10.1063/1.4710527)
7. Hell S, Reiner G, Cremer C, Stelzer EHK. 1993 Aberrations in confocal fluorescence microscopy induced by mismatches in refractive index. *J. Microsc.* **169**, 391–405. (doi:10.1111/jmi.1993.169.issue-3)
8. Ji N, Sato TR, Betzig E. 2012 Characterization and adaptive optical correction of aberrations during in vivo imaging in the mouse cortex. *Proc. Natl Acad. Sci. USA* **109**, 22–27. (doi:10.1073/pnas.1109202108)
9. Dong CY, Koenig K, So PTC. 2003 Characterizing point spread functions of two-photon fluorescence microscopy in turbid medium. *J. Biomed. Opt.* **8**, 450–459. (doi:10.1117/1.1578644)
10. Booth MJ. 2014 Adaptive optical microscopy: the ongoing quest for a perfect image. *Light: Sci. Appl.* **3**, e165–e165. (doi:10.1038/lsa.2014.46)

11. Tao X, Fernandez B, Azucena O, Fu M, Garcia D, Zuo Y, Chen DC, Kubby J. 2011 Adaptive optics confocal microscopy using direct wavefront sensing. *Opt. Lett.* **36**, 1062–1064. (doi:10.1364/OL.36.001062)
12. Betzig E, Patterson GH, Sougrat R, Lindwasser OW, Olenych S, Bonifacino JS, Davidson MW, Lippincott-Schwartz J, Hess HF. 2006 Imaging intracellular fluorescent proteins at nanometer resolution. *Science* **313**, 1642–1645. (doi:10.1126/science.1127344)
13. Hess ST, Girirajan TPK, Mason MD. 2006 Ultra-high resolution imaging by fluorescence photoactivation localization microscopy. *Biophys. J.* **91**, 4258–4272. (doi:10.1529/biophysj.106.091116)
14. Madec PY. 2012 Overview of deformable mirror technologies for adaptive optics and astronomy. In *Adaptive optics systems III*, vol. 8447, p. 844705. Amsterdam, The Netherlands: International Society for Optics and Photonics.
15. Heilemann M, van de Linde S, Schüttpelz M, Kasper R, Seefeldt B, Mukherjee A, Tinnefeld P, Sauer M. 2008 Subdiffraction-resolution fluorescence imaging with conventional fluorescent probes. *Angew. Chem. Int. Ed.* **47**, 6172–6176. (doi:10.1002/anie.v47:33)
16. Rust MJ, Bates M, Zhuang X. 2006 Stochastic optical reconstruction microscopy (STORM) provides sub-diffraction-limit image resolution. *Nat. Methods* **3**, 793–795. (doi:10.1038/nmeth929)
17. Huang B, Wang W, Bates M, Zhuang X. 2008 Three-dimensional super-resolution imaging by stochastic optical reconstruction microscopy. *Science* **319**, 810–813. (doi:10.1126/science.1153529)
18. Holtzer L, Meckel T, Schmidt T. 2007 Nanometric three-dimensional tracking of individual quantum dots in cells. *Appl. Phys. Lett.* **90**, 053902. (doi:10.1063/1.2437066)
19. Aristov A, Lelandais B, Rensen E, Zimmer C. 2018 ZOLA-3D allows flexible 3D localization microscopy over an adjustable axial range. *Nat. Commun.* **9**, 2409. (doi:10.1038/s41467-018-04709-4)
20. Pavani SRP, Thompson MA, Biteen JS, Lord SJ, Liu N, Twieg RJ, Piestun R, Moerner WE. 2009 Three-dimensional, single-molecule fluorescence imaging beyond the diffraction limit by using a double-helix point spread function. *Proc. Natl Acad. Sci. USA* **106**, 2995–2999. (doi:10.1073/pnas.0900245106)
21. Martens KJA, Jabermoradi A, Yang S, Hohlbein J. 2020 Integrating engineered point spread functions into the phasor-based single-molecule localization microscopy framework. *Methods* **193**, 107–115. (doi:10.1016/j.ymeth.2020.07.010)
22. Hohlbein J. 2021 Single-molecule localization microscopy as an emerging tool to probe multiscale food structures. *Food Struct.* **30**, 100236. (doi:10.1016/j.foostr.2021.100236)
23. Martens KJA *et al.* 2019 Visualisation of dCas9 target search in vivo using an open-microscopy framework. *Nat. Commun.* **10**, 3552. (doi:10.1038/s41467-019-11514-0)
24. Douglass KM, Sieben C, Archetti A, Lambert A, Manley S. 2016 Super-resolution imaging of multiple cells by optimized flat-field epi-illumination. *Nat. Photonics* **10**, 705–708. (doi:10.1038/nphoton.2016.200)
25. Scholtens TM, Schreuder F, Ligthart ST, Swennenhuis JF, Tibbe AGJ, Greve J, Terstappen LWMM. 2011 CellTracks TDI: An image cytometer for cell characterization. *Cytometry Part A* **79A**, 203–213. (doi:10.1002/cyto.a.v79a.3)
26. Deschamps J, Rowald A, Ries J. 2016 Efficient homogeneous illumination and optical sectioning for quantitative single-molecule localization microscopy. *Opt. Express* **24**, 28 080–28 090. (doi:10.1364/OE.24.028080)
27. Kwakwa K, Savell A, Davies T, Munro I, Parrinello S, Purbhoo MA, Dunsby C, Neil MAA, French PMW. 2016 easySTORM: a robust, lower-cost approach to localisation and TIRF microscopy. *J. Biophotonics* **9**, 948–957. (doi:10.1002/jbio.v9.9)
28. Ma H, Fu R, Xu J, Liu Y. 2017 A simple and cost-effective setup for super-resolution localization microscopy. *Sci. Rep.* **7**, 1542. (doi:10.1038/s41598-017-01606-6)
29. Mau A, Friedl K, Leterrier C, Bourg N, Lévêque-Fort S. 2020 Fast scanned widefield scheme provides tunable and uniform illumination for optimized SMLM on large fields of view. *bioRxiv*, p. 2020.05.08.083774. (doi:10.1101/2020.05.08.083774)
30. Khaw I, Croop B, Tang J, Möhl A, Fuchs U, Han KY. 2018 Flat-field illumination for quantitative fluorescence imaging. *Opt. Express* **26**, 15 276–15 288. (doi:10.1364/OE.26.015276)

31. Stehr F, Stein J, Schueder F, Schwille P, Jungmann R. 2019 Flat-top TIRF illumination boosts DNA-PAINT imaging and quantification. *Nat. Commun.* **10**, 1268. (doi:10.1038/s41467-019-09064-6)
32. Siemons ME, Hanemaaijer NAK, Kole MHP, Kapitein LC. 2021 Robust adaptive optics for localization microscopy deep in complex tissue. *Nat. Commun.* **12**, 3407. (doi:10.1038/s41467-021-23647-2)
33. Yang S, Verhoeff AA, Merkx DWH, van Duynhoven JPM, Hohlbein J. 2020 Quantitative spatiotemporal mapping of lipid and protein oxidation in mayonnaise. *Antioxidants* **9**, 1278. (doi:10.3390/antiox9121278)
34. Depree JA, Savage GP. 2001 Physical and flavour stability of mayonnaise. *Trends Food Sci. Technol.* **12**, 157–163. (doi:10.1016/S0924-2244(01)00079-6)
35. Castellani O, Belhomme C, David-Briand E, Guérin-Dubiard C, Anton M. 2006 Oil-in-water emulsion properties and interfacial characteristics of hen egg yolk phosvitin. *Food Hydrocolloids* **20**, 35–43. (doi:10.1016/j.foodhyd.2005.02.010)
36. Zhang X, Qiu N, Geng F, Ma M. 2011 Simply and effectively preparing high-purity phosvitin using polyethylene glycol and anion-exchange chromatography. *J. Sep. Sci.* **34**, 3295–3301. (doi:10.1002/jssc.v34.22)
37. Berton-Carabin CC, Ropers MH, Genot C. 2014 Lipid oxidation in oil-in-water emulsions: involvement of the interfacial layer. *Compr. Rev. Food Sci. Food Saf.* **13**, 945–977. (doi:10.1111/crf3.2014.13.issue-5)
38. Luca GMRD *et al.* 2013 Re-scan confocal microscopy: scanning twice for better resolution. *Biomed. Opt. Express* **4**, 2644–2656. (doi:10.1364/BOE.4.002644)
39. Ovesný M, Křížek P, Borkovec J, Švindrych Z, Hagen GM. 2014 ThunderSTORM: a comprehensive ImageJ plug-in for PALM and STORM data analysis and super-resolution imaging. *Bioinformatics* **30**, 2389–2390. (doi:10.1093/bioinformatics/btu202)
40. Schindelin J *et al.* 2012 Fiji: an open-source platform for biological-image analysis. *Nat. Methods* **9**, 676–682. (doi:10.1038/nmeth.2019)
41. Martens KJA, Bader AN, Baas S, Rieger B, Hohlbein J. 2018 Phasor based single-molecule localization microscopy in 3D (pSMLM-3D): an algorithm for MHz localization rates using standard CPUs. *J. Chem. Phys.* **148**, 123311. (doi:10.1063/1.5005899)
42. Nieuwenhuizen RPJ, Lidke KA, Bates M, Puig DL, Grünwald D, Stallinga S, Rieger B. 2013 Measuring image resolution in optical nanoscopy. *Nat. Methods* **10**, 557–562. (doi:10.1038/nmeth.2448)
43. Yuen HK, Princen J, Dlingworth J, Kittler J. 1989 A comparative study of hough transform methods for circle finding. In *Proc. of the Alvey Vision Conf. 1989*, Reading, UK, 25–28 September 1989, pp. 29.1–29.6. Reading, UK: Alvey Vision Club.
44. Ries J. 2020 SMAP: a modular super-resolution microscopy analysis platform for SMLM data. *Nat. Methods* **17**, 870–872. (doi:10.1038/s41592-020-0938-1)
45. Jimenez A, Friedl K, Leterrier C. 2020 About samples, giving examples: optimized single molecule localization microscopy. *Methods* **174**, 100–114. (doi:10.1016/j.ymeth.2019.05.008)
46. Banterle N, Bui KH, Lemke EA, Beck M. 2013 Fourier ring correlation as a resolution criterion for super-resolution microscopy. *J. Struct. Biol.* **183**, 363–367. (doi:10.1016/j.jsb.2013.05.004)
47. Schuster S, Bernewitz R, Guthausen G, Zapp J, Greiner AM, Köhler K, Schuchmann HP. 2012 Analysis of $W_1/O/W_2$ double emulsions with CLSM: Statistical image processing for droplet size distribution. *Chem. Eng. Sci.* **81**, 84–90. (doi:10.1016/j.ces.2012.06.059)
48. van Duynhoven JPM, Goudappel GJW, van Dalen G, van Bruggen PC, Blonk JCG, Eijkelenboom APaM. 2002 Scope of droplet size measurements in food emulsions by pulsed field gradient NMR at low field. *Magn. Reson. Chem.* **40**, S51–S59. (doi:10.1002/(ISSN)1097-458X)